

Microstructure evolution and strengthening mechanism of high-performance powder metallurgy TA15 titanium alloy by hot rolling

Ying Gao, Ce Zhang, Jiazhen Zhang, and Xin Lu

Cite this article as:

Ying Gao, Ce Zhang, Jiazhen Zhang, and Xin Lu, Microstructure evolution and strengthening mechanism of high-performance powder metallurgy TA15 titanium alloy by hot rolling, *Int. J. Miner. Metall. Mater.*, 31(2024), No. 6, pp. 1426-1436. <https://doi.org/10.1007/s12613-023-2809-0>

View the article online at [SpringerLink](#) or [IJMMM Webpage](#).

Articles you may be interested in

Bo-ren Ke, Yu-chen Sun, Yong Zhang, Wen-rui Wang, Wei-min Wang, Pei-yan Ma, Wei Ji, and Zheng-yi Fu, [Powder metallurgy of high-entropy alloys and related composites: A short review](#), *Int. J. Miner. Metall. Mater.*, 28(2021), No. 6, pp. 931-943. <https://doi.org/10.1007/s12613-020-2221-y>

Mehmet Akif Erden and Fatih Aydın, [Wear and mechanical properties of carburized AISI 8620 steel produced by powder metallurgy](#), *Int. J. Miner. Metall. Mater.*, 28(2021), No. 3, pp. 430-439. <https://doi.org/10.1007/s12613-020-2046-8>

Tao Lan, Yi-hui Jiang, Xiao-jun Zhang, Fei Cao, and Shu-hua Liang, [Competitive precipitation behavior of hybrid reinforcements in copper matrix composites fabricated by powder metallurgy](#), *Int. J. Miner. Metall. Mater.*, 28(2021), No. 6, pp. 1090-1096. <https://doi.org/10.1007/s12613-020-2052-x>

Wei Long, Song Zhang, Yi-long Liang, and Mei-gui Ou, [Influence of multi-stage heat treatment on the microstructure and mechanical properties of TC21 titanium alloy](#), *Int. J. Miner. Metall. Mater.*, 28(2021), No. 2, pp. 296-304. <https://doi.org/10.1007/s12613-020-1996-1>

Parnia Parvizian, Maryam Morakabati, and Saeed Sadeghpour, [Effect of hot rolling and annealing temperatures on the microstructure and mechanical properties of SP-700 alloy](#), *Int. J. Miner. Metall. Mater.*, 27(2020), No. 3, pp. 374-383. <https://doi.org/10.1007/s12613-019-1922-6>

Xiang Zeng, Jie Teng, Jin-gang Yu, Ao-shuang Tan, Ding-fa Fu, and Hui Zhang, [Fabrication of homogeneously dispersed graphene/Al composites by solution mixing and powder metallurgy](#), *Int. J. Miner. Metall. Mater.*, 25(2018), No. 1, pp. 102-109. <https://doi.org/10.1007/s12613-018-1552-4>



IJMMM WeChat



QQ author group

Microstructure evolution and strengthening mechanism of high-performance powder metallurgy TA15 titanium alloy by hot rolling

Ying Gao¹⁾, Ce Zhang^{2),✉}, Jiazhen Zhang^{1,2)}, and Xin Lu^{1,2),✉}

1) Beijing Advanced Innovation Center for Materials Genome Engineering, State Key Laboratory for Advanced Metals and Materials, Institute for Advanced Materials and Technology, University of Science and Technology Beijing, Beijing 100083, China

2) National Engineering Research Center for Advanced Rolling Technology, National Engineering Research Center for Flat Rolling Equipment, Institute of Engineering Technology, University of Science and Technology Beijing, Beijing 100083, China

(Received: 2 September 2023; revised: 12 December 2023; accepted: 13 December 2023)

Abstract: Hot deformation of sintered billets by powder metallurgy (PM) is an effective preparation technique for titanium alloys, which is more significant for high-alloying alloys. In this study, Ti–6.5Al–2Zr–Mo–V (TA15) titanium alloy plates were prepared by cold pressing sintering combined with high-temperature hot rolling. The microstructure and mechanical properties under different process parameters were investigated. Optical microscope, electron backscatter diffraction, and others were applied to characterize the microstructure evolution and mechanical properties strengthening mechanism. The results showed that the chemical compositions were uniformly diffused without segregation during sintering, and the closing of the matrix craters was accelerated by increasing the sintering temperature. The block was hot rolled at 1200°C with an 80% reduction under only two passes without annealing. The strength and elongation of the plate at 20–25°C after solution and aging were 1247 MPa and 14.0%, respectively, which were increased by 24.5% and 40.0%, respectively, compared with the as-sintered alloy at 1300°C. The microstructure was significantly refined by continuous dynamic recrystallization, which was completed by the rotation and dislocation absorption of the substructure surrounded by low-angle grain boundaries. After hot rolling combined with heat treatment, the strength and plasticity of PM-TA15 were significantly improved, which resulted from the dense, uniform, and fine recrystallization structure and the synergistic effect of multiple slip systems.

Keywords: elemental powder; powder metallurgy; titanium alloy; hot rolling; strength and plasticity

1. Introduction

Pure-Ti and titanium alloys have been extensively used in aerospace, marine engineering, biomedicine, and other fields because of their high specific strength, high/low-temperature resistance, better corrosion resistance, and excellent biocompatibility [1–4]. Traditional ingot metallurgy blocks were formed through vacuum melting combined with a hot deformation process, which contained a lower material usage rate and a smaller window of hot deformation. High deformation resistance and component segregation make it difficult and costly to prepare high-alloying titanium alloys using traditional processes [5–7]. Powder metallurgy (PM) is an important method for fabricating low-cost titanium alloys including rods, tubes, plates, and other alloy products combined with hot deformation, and its near-net forming characteristics greatly improve the utilization rate of materials [8–9]. The fine uniform structure and high-temperature stability of PM sintered billets significantly increase the hot formability and broaden the window of hot processing [10–11].

Hot deformation and subsequent heat treatment of PM ti-

tanium alloys have received extensive attention. The hot rolling process with PM blocks has been studied for pure Ti and its alloys, and there are already some plates of titanium alloys for practical applications [12–13]. Hong *et al.* [14] fabricated high-density strips by powder direct rolling with different morphologies and sizes of mixed powder. They showed that the density increased with the reduction of powder particle size, rolling speed, and gap, and similar conclusions could be obtained in other work [15]. CSIRO in Australia fabricated pure-Ti or Ti–6Al–4V sheets using powder direct rolling methods combined with annealing treatment with pre-alloying and blending element powders. The oxygen content, tensile strength, and plasticity of the pure-Ti sheet were 0.12wt%, 517–520 MPa, and 20%–27%, respectively, which met the requirements of the ASTM B265 standard in process and properties [16–19]. Gogaev *et al.* [20–21] further optimized the powder rolling process and applied the high deformation stress asymmetric rolling method to prepare titanium alloy strips, which possessed better mechanical properties, enhanced contact quality between the powders, and significantly improved plasticity and fatigue resistance. O’Flynn and Corbin [22] prepared titanium strips

✉ Corresponding authors: Ce Zhang E-mail: zhangce@ustb.edu.cn; Xin Lu E-mail: luxin@ustb.edu.cn

© University of Science and Technology Beijing 2024

by direct cold rolling based on powder-sintered billets, and the thickness was reduced to 0.15–0.30 mm with a density of more than 99%. Furthermore, Xu *et al.* [23] explored the application of cold pressing sintering and hot rolling on Ti–5Al–3Mo–2Fe alloy, which possessed heterogeneous grains of residual β , acicular secondary α , and equiaxial primary α phases. The strength and elongation at 20–25°C reached 1422 MPa and 8.5%, respectively. It has also been successfully applied to the intake valve of automobile engines. Govender *et al.* [24] further optimized the process, which adopted the continuous sintering process under the protection of argon instead of high vacuum sintering. They obtained highly dense and highly plastic titanium strips after sintering at 1100–1200°C for 30–90 min. Recently, Zhou *et al.* [25] prepared PM-Ti containing high oxygen and high plasticity by hot rolling. The oxygen content of the PM-Ti plate reached 0.56wt%, which was far higher than the oxygen threshold of 0.33wt%. Its tensile strength and plasticity were 824 MPa and 15%, respectively (higher than the traditional pure titanium plate). The complete dissolution of the O and Zr atoms changed the lattice constant and improved the tensile strength, and the plasticity was enhanced by fine equiaxed recrystallized grains. Additionally, a finer secondary α structure was obtained than that of the traditional solution treatment, which was connected with the appropriate composition fluctuation by rapid heat treatment in PM plates, which broke the strength–plasticity trade-off [26]. In summary, powder hot rolling is beneficial for broadening the hot processing window, reducing rolling pressure, increasing rolling speed, and improving the density and mechanical properties of titanium alloys. The combination of PM technology and the hot deformation process is a valuable method for fabricating low-cost and high-performance titanium alloys. However, these studies focus on low-alloying alloys with fewer components, such as pure-Ti, Ti–6Al–4V (TC4),

and others. Additionally, there are few reports on the hot deformation of multicomponent and high-alloying PM titanium alloys, and the sintering process and hot deformation mechanism need to be further studied.

In this study, a medium-temperature Ti–6.5Al–2Zr–Mo–V (TA15) alloy was prepared by combining PM technology, high-temperature hot rolling, and heat treatment. The influence of sintering parameters on the microstructure morphology, phase compositions, and mechanical properties was investigated. Consequently, the evolution mechanism of the microstructure and strengthening mechanism of the mechanical properties were revealed. This study also described the feasibility of fabricating low-cost and high-performance TA15 alloys using PM and hot rolling.

2. Experimental

2.1. Powder and sample fabrication

The irregular hydridehydrogenated Ti (HDH-Ti) and Al₆₀V₄₀ powders were purchased from Tian Tai Long (Tianjin) Metal Materials Co., Ltd., China. The spherical Al powder was provided by Angang Industrial Fine Aluminum Powder Co., Ltd., China, with a size of 5–10 μm in a purity of 99.5wt%. The irregular Zr powder was purchased from Beijing Xing Rong Yuan Technology Co., Ltd., China, with a size of 38–48 μm in a purity of 99.5wt%. The Mo powder was supplied by Shanghai Macklin Biochemical Technology Co., Ltd., China, with a size of 1–5 μm in a purity of 99.5wt%. As shown in Fig. 1, raw material powders of TA15 titanium alloy were weighed according to the ratio of chemical compositions in a glovebox (Shanghai Mikrouna) with high-purity argon ($\geq 99.999\%$). These powders were put into a polyethylene plastic cylindrical bottle and mechanically blended in a double-roller blender (GMS5-4, Changsha Miqi Equipment, China) at a speed of 150 r/min for 12 h and a 1:1

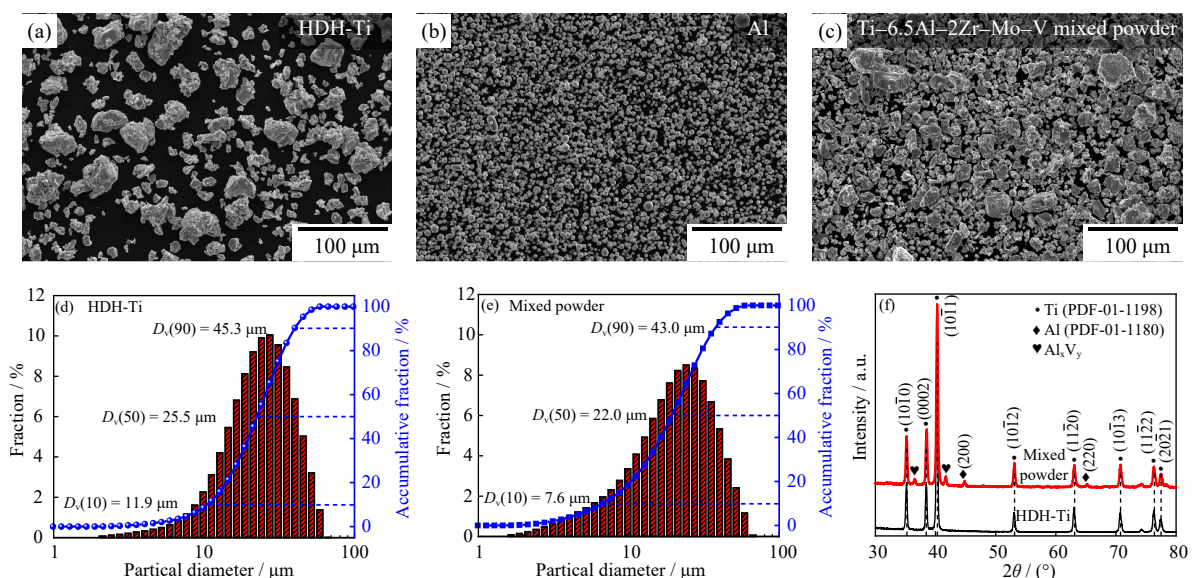


Fig. 1. Morphology of (a) HDH-Ti, (b) Al, and (c) TA15 mixed powder; particle sizes of (d) HDH-Ti and (e) TA15 mixed powder; (f) phase compositions of HDH-Ti and TA15 mixed powder. $D_v(10)$, $D_v(50)$, and $D_v(90)$ were the corresponding diameter value of the horizontal coordinate when the cumulative vertical distribution of 10%, 50% and 90%, respectively.

mass ratio between ZrO_2 balls and powders. The green compacts ($\phi 53 \text{ mm} \times 110 \text{ mm}$) were compacted using a cold isostatic pressing technique (CIP200/500-300, Sichuan Bai Rui Long Equipment, China) under 250 MPa for 10 min with the mixed powders. Then, the compacts were sintered at 1200, 1250, 1300, and 1350°C for 120 min with 5°C/min of heating rate in high-purity Ar (600 mL/min). The effects of element content on the phase transition temperature of PM-TA15 were calculated using the differential scanning calorimetry (DSC, NETZSCH STA 449 F3, Germany) method, and the phase transition temperature between α -Ti and β -Ti in PM-TA15 was approximately 1050°C, which was evidence for the selection temperature of rolling and heat treatment. The block was then hot rolled by a multifunctional hot rolling machine (Z1342, Shanxi Ya Yan equipment, China) at 1200°C with an 80% reduction from 36 to 7.2 mm in height under only two passes without annealing. Finally, the plate was subjected to solution and aging heat treatment in a box furnace (TC50L-14, Wuxi Marit Technology, China), in which the parameters were heated to 975°C and kept for 30 min with water cooling and heated to 850°C and kept for 120 min with air cooling.

2.2. Characterization

Scanning electron microscopy (SEM, FEI Quanta 450F, Thermo Field, USA) was performed to characterize the morphology of the powder at 20-kV acceleration voltage. A laser particle size analyzer (Mastersizer 3000, Malvern Panaco, UK) was implemented to measure the powder size. The interstitial element contents, including O, N, and H of the powder and alloys, were detected by an O–N–H analyzer (LECO TCH-600, GOEPE, USA). A Bruker D8 Advance X-ray diffractometer (XRD, Bruker, Germany) was used to determine the phase compositions of the powder and alloys at 40 kV and 40 mA with 2°/min of scanning speed. The morphology of the as-sintered, as-rolled, and as-treated alloys was characterized using a microscope (LEXT OLS4100, Olympus, Japan), where these specimens were prepared by mechanical polishing and then etched using the Kroll reagent. The density of the alloys was then examined using the Archimedes method. A JXA-8530F electron probe X-ray mi-

croanalyzer (EPMA, JEOL, Japan) was used to estimate the element distribution of the PM-TA15 sintered alloy. Additionally, an electron backscatter diffraction (EBSD) was conducted to characterize the microstructure of the alloys equipped with an AZtec system and Oxford Instruments in JSM-7900F SEM (JEOL, Japan). The samples were electrochemically polished with a solution of ethanol, butoxyethanol, and perchloric acid for 20–60 s at 5.0 V. Two standard tensile samples within a 15-mm tensile distance were cut by wire-cutting equipment in PM-TA15 alloys. The standard samples were then examined on a universal testing machine (CMT4204, CMT) at 20–25°C with a strain rate of $1 \times 10^{-2} \text{ s}^{-1}$, and the fracture morphology was also studied by FEI Quanta 450F SEM.

3. Results

3.1. Powder characterization

Fig. 1(a)–(c) shows the morphology of the elemental powders for the Ti–6.5Al–2Zr–Mo–V alloy. Except for the spherical powder of Al, the other powders were irregular and angular. HDH-Ti and other elemental powders could be seen in the mixed powder, indicating that the powder was evenly mixed. As shown in Fig. 1(d) and (e), the particle sizes of HDH-Ti and TA15 mixed powders were normally distributed, and the mean size was 25.5 and 22.0 μm , respectively. The reduction in particle size is attributed to the adulteration of fine Al and Mo powders. As shown in Fig. 1(f), the phase of HDH-Ti powder was the hcp-Ti phase without other miscellaneous phases, and the main phase of TA15 mixed powder was also the hcp-Ti phase. The diffraction peaks of Al and Al_xV_y powder could also be detected, confirming that the powder was evenly mixed. As presented in Table 1, the contents of O, N, and H interstitial elements in HDH-Ti matrix powder were 0.20wt%, 0.026wt%, and 0.012wt%, respectively, while the contents of O, N, and H elements in the TA15 mixed powders were 0.28wt%, 0.029wt%, and 0.030wt%, respectively. The increase in the element content is attributed to the adulteration of other alloying powders and the mechanical mixing process.

Table 1. Particle size and interstitial element content of raw powders

Powder	Particle size / μm			Interstitial element / wt%		
	$D_v(10)$	$D_v(50)$	$D_v(90)$	O	N	H
HDH-Ti	11.9	25.5	45.3	0.20	0.026	0.012
Mixed powder	7.6	22.0	43.0	0.28	0.029	0.030

3.2. Phase and microstructure

Fig. 2(a) shows the XRD spectrum of the TA15 alloys. It shows that the phase structure of PM-TA15 titanium alloy comprised hcp-Ti and a few β -Ti phases. At high angles in the range of 50°–80°, the intensity of the diffraction peaks decreased with increasing sintering temperature, and some peaks even disappeared between 1250–1350°C. The pre-

ferred orientation peak was $(10\bar{1}1)_\alpha$, and the $(10\bar{1}1)_\alpha$ peak shifted to a lower angle because of the increase in interplanar crystal spacing according to the Bragg equation. In the TA15 alloy, Al was the principal alloying element belonging to the α -Ti phase stable element, and the increase in the spacing was due to the solid solution of Al atoms [27]. After hot rolling and heat treatment, the preferred orientation peak was still $(10\bar{1}1)_\alpha$, and the high-angle diffraction peaks in the

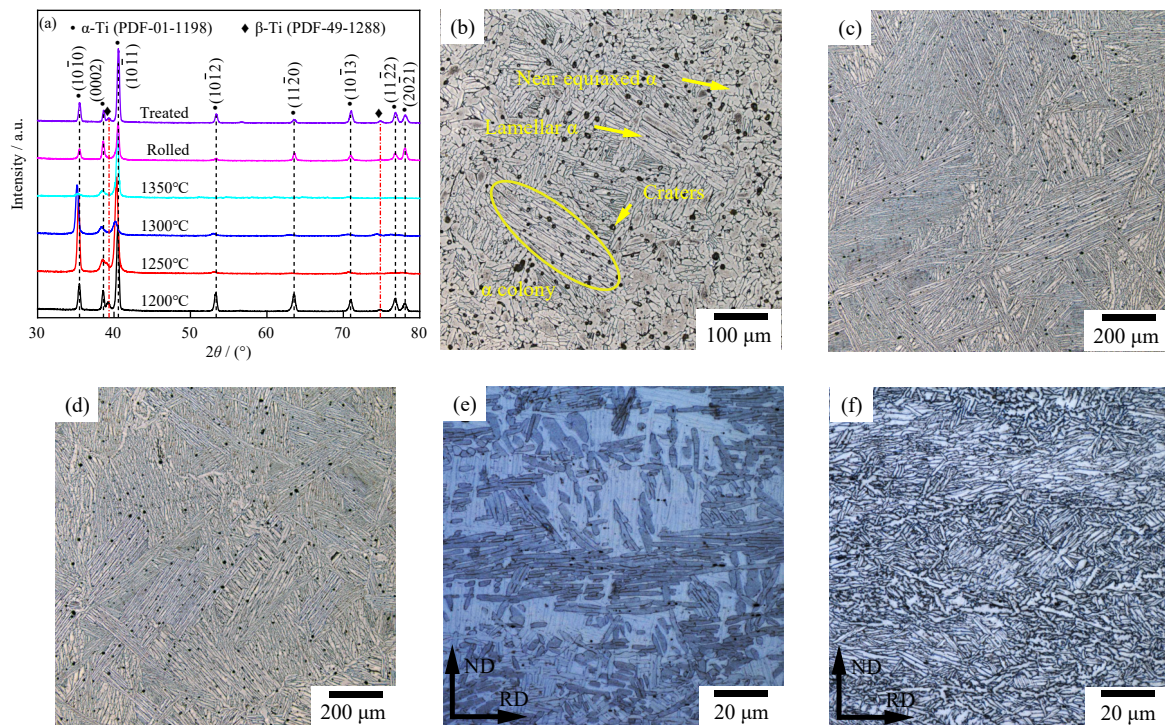


Fig. 2. XRD spectrum and OM images of the PM-TA15 sintered and rolled samples: (a) XRD spectrum, (b) 1200°C, (c) 1300°C, (d) 1350°C, (e) as-rolled, and (f) as-treated. ND—normal direction; RD—rolling direction.

range of 50°–80° could also be observed.

Fig. 2(b)–(f) shows the metallographic morphology of TA15 alloys. Sintering at 1200°C, there were many craters in the alloy, and the density was the lowest (98.0%). At 1300°C, the size and number of craters decreased significantly, and the density of the alloy increased to 98.9%, which was the highest value. Meanwhile, at 1350°C, the size and number of craters showed no significant change compared with that at 1300°C, and the density of this alloy was 98.8%. The increase in the sintering temperature could effectively eliminate craters in PM-TA15, and the increasing density is mainly attributed to the closing of the residual craters [28]. After hot rolling and heat treatment (Fig. 2(e) and (f)), the craters were completely closed, where the alloy reached a fully dense state with 100% density, and the effective bearing area and the continuity of the microstructure were further increased. Moreover, the alloy at 1200°C possessed near equiaxed structure, lamellar structure, and some lamellar colony. The alloy presented only lamellar structure, and the size of lamellae increased with increasing sintering temperature. As shown in Fig. 2(e) and (f), the grains were significantly refined, the width and length of the lamellar were also reduced, and the obvious fiber morphology along the rolling direction (RD) could be observed. After heat treatment, recrystallization occurred, and the near equiaxed and lamellar structures coexisted in the alloy.

Fig. 3 shows the EPMA results of PM-TA15 alloy as-sintered at 1300°C. The backscattered electron (BSE) image (Fig. 3(a)) was mainly divided into two regions containing the gray lamellar and bright-white lamellar interface regions. As shown in Fig. 3(b), the Ti element existed in the entire field of view, and the content of the Ti element in the lamella

was higher than that at the lamellar interface. Al was concentrated in the lamellar region (Fig. 3(c)), which is an α stable element, and the lamellar region could be identified as α -Ti. As shown in Fig. 3(d), Zr was evenly distributed throughout the field of view as a neutral element. The Mo and V elements were concentrated at the lamellar interface as a β -stable element (Fig. 3(e) and (f)), which corresponded to the XRD spectrum of the alloy at 1300°C (Fig. 2(a)) with fewer β -Ti diffraction peaks. Moreover, Ti, Al, Zr, Mo, and V elements belonging to the TA15 alloy could be clearly observed, and the elements were uniformly diffused and dispersed in the alloy without element enrichment or segregation.

Fig. 4 shows the EBSD images containing inverse pole figures (IPF) and grain boundaries (GBs) mappings and the results of the PM-TA15 alloy at 1300°C and the as-treated sample. The red and black lines in the IPF and GB mappings represent the low-angle grain boundaries (LAGBs) and high-angle grain boundaries (HAGBs). As shown in Fig. 4(a), (c), and (e), the PM-TA15 alloy at 1300°C has an obvious uniform lamellar structure without any orientation gradient (Fig. 4(a1)), and the frequency of LAGBs was 16.2%. As shown in Fig. 4(b), (d), and (f) of the as-treated alloys in the RD–ND selected plane, the grains were significantly refined with a fine lamellar and near equiaxed structure with clear crystalline orientation (Fig. 4(b1)). The texture characteristics are shown in Fig. 4(a1) and (b1). The as-sintered sample had no texture characteristics. However, a higher intensity of $\langle 0001 \rangle_a // RD$ texture and a lower strength of $\langle 10\bar{1}0 \rangle_a // RD$ texture could be detected in the as-treated alloy. As shown in Fig. 4(c)–(f), the GBs distribution mapping verified the increase of LAGBs after hot rolling and heat treatment, and the GB angle orientation distribution in the alloys indicated obvi-

ous peaks around the 10°, 60°, and 90° sites, respectively, with the related rotation axis orientations (Taylor axis) were $\langle 0001 \rangle > 10.5^\circ$, $\langle 11\bar{2}0 \rangle > 59^\circ\text{--}63^\circ$, and $\langle 11\bar{2}0 \rangle > 90^\circ$, respectively.

The distribution of the local average strain difference in the alloys was investigated using kernel average misorientation (KAM) mapping (Fig. 5). As shown in Fig. 5(a) and (b),

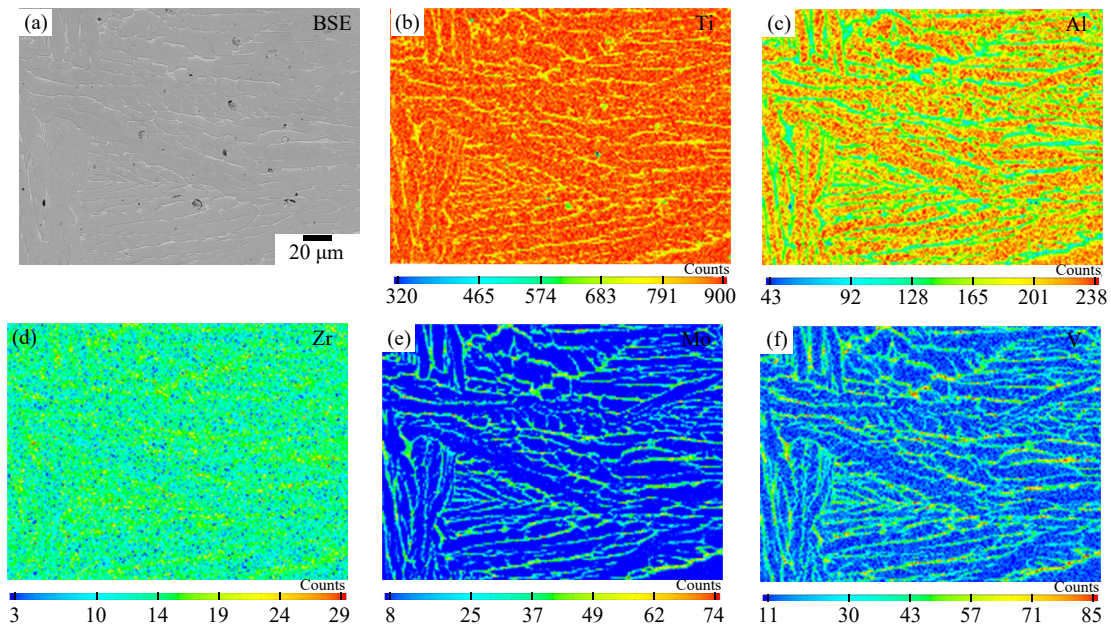


Fig. 3. EPMA images with the element distribution of 1300°C sintered samples: (a) BSE morphology, (b) Ti, (c) Al, (d) Zr, (e) Mo, and (f) V.

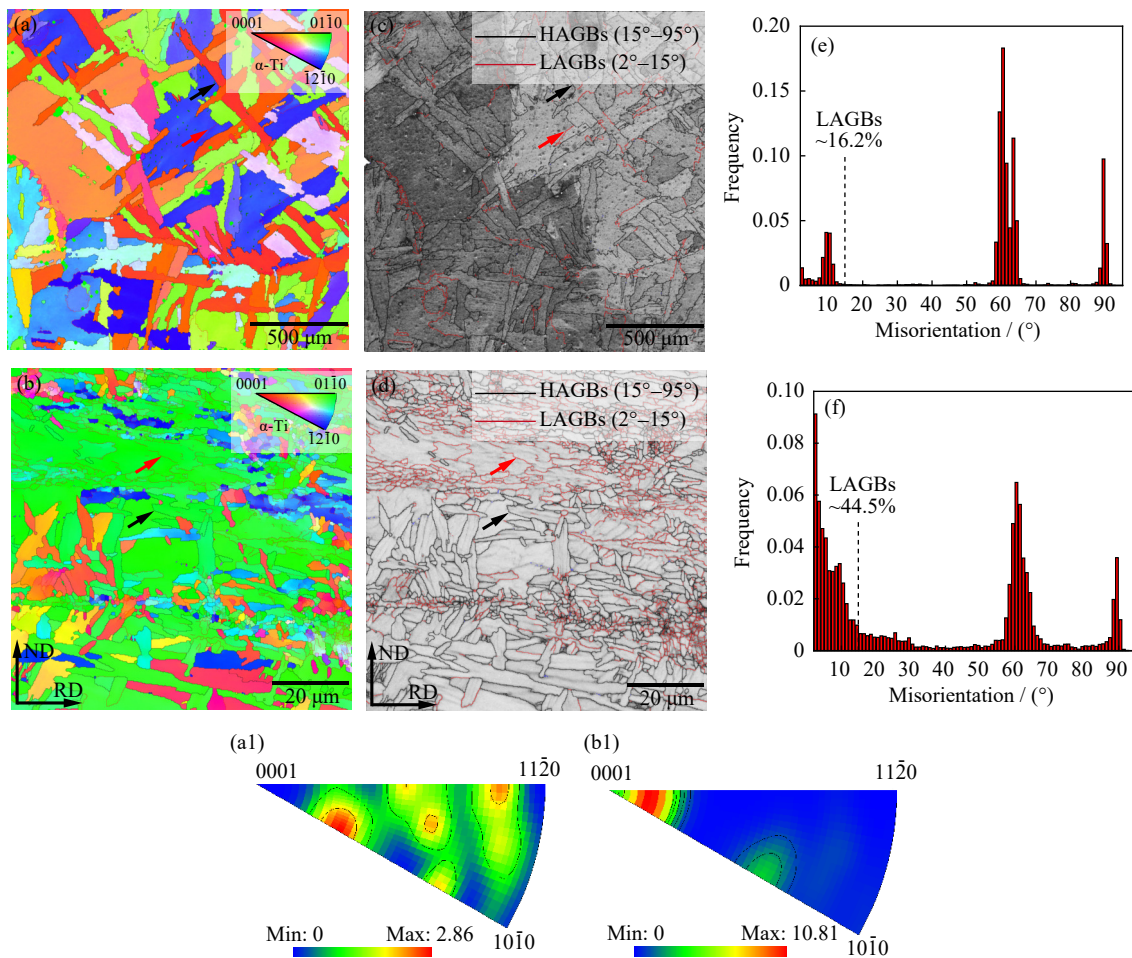


Fig. 4. EBSD images containing (a, b, a1, b1) IPF and (c–f) GB mappings and results for different samples: (a, a1, c, e) sintered at 1300°C; (b, b1, d, f) as-treated.

the residual strain intensity of the PM-TA15 alloy sintered at 1300°C was very low, and the intensity of the as-treated alloy was higher. Especially at the fine grain location, LAGBs (Fig. 4(b) and (d)) usually existed in regions with high KAM values (Fig. 5(b)). Fig. 5(c) and (d) shows the grain type distribution of PM-TA15 alloys related to the forming mechanism of the grains. The grain type of PM-TA15 sintered at 1300°C contained sub-structured grains accounting for 76.0%, the recrystallized grains accounting for 23.1%, and the deformed grains were basically absent. In the as-treated samples, the sub-structured grains decreased to 69.5%, and the proportion of recrystallized and deformed grains increased to 25.6% and 4.9%, respectively. The increase in recrystallized and deformed grains provided more nucleation sites for dynamic recrystallization and grain refinement [27].

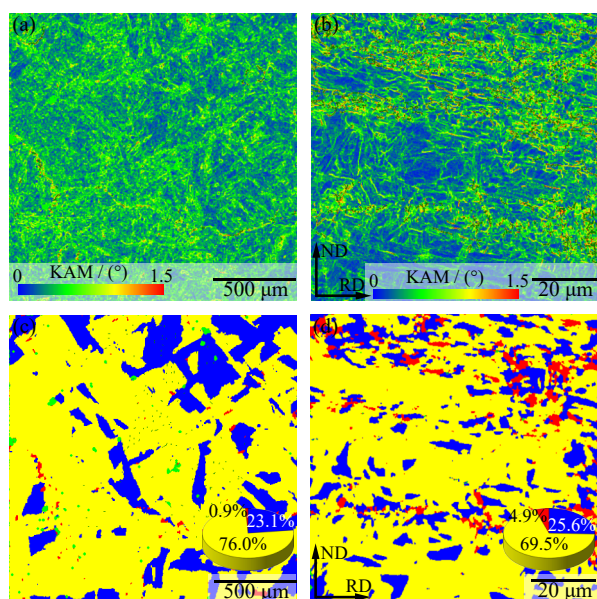


Fig. 5. (a, b) EBSD images of KAM and (c, d) grain type distribution mappings for different samples: (a, c) sintered at 1300°C; (b, d) as-treated.

Fig. 6 shows the Schmid factor (SF) of different slip systems in the PM-TA15 as-treated alloy. Here, every mapping represents different crystal orientations of the connecting slip system, and the average value of SF was calculated. As shown in Fig. 6(b), the average SF value of $(10\bar{1}0)\langle\bar{1}\bar{2}10\rangle$ prismatic slip was 0.186, which was lower than that of other slip systems resulting from the small critical resolved shear stress (CRSS) [27]. These grains in the prismatic slip system, which had an importantly selected $\langle 0001\rangle//RD$ orientation, could still facilitate the activation of the slip under hot rolling. As shown in Fig. 6(b) and (d), the area with a lower SF value in prismatic slip $\langle\bar{a}\rangle$ had a higher SF value in pyramidal slip $\langle\bar{c} + \bar{a}\rangle$. Meanwhile, these grains in the slip systems still had stronger $\langle 0001\rangle$ orientation connected with the stronger basal texture in the as-treated alloys. Moreover, the average SF value of $(0001)\langle 11\bar{2}0\rangle$ basal slip (Fig. 6(a)) was 0.281, in which the higher SF value region in the $(0001)\langle 11\bar{2}0\rangle$ basal slip was similar to that of the $(10\bar{1}1)\langle 1\bar{2}10\rangle$ pyramidal slip system (Fig. 6(c)). This con-

firms that the hot rolling deformation of PM-TA15 alloy at high temperatures originated from the synergistic effects of different types of slip systems.

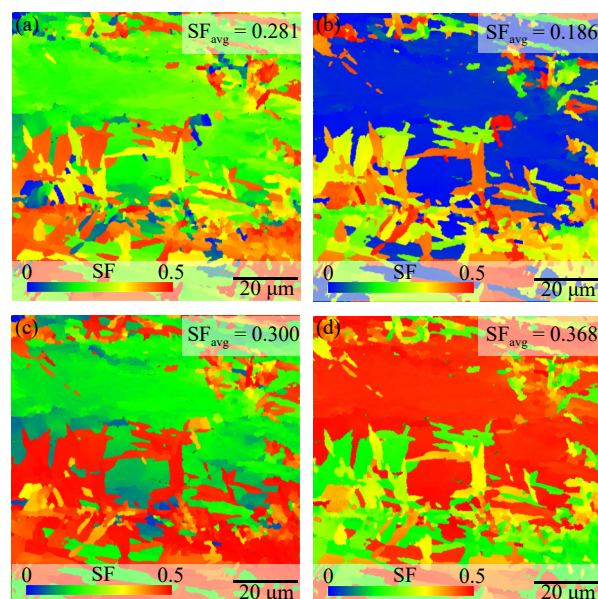


Fig. 6. Schmid factor mappings of the as-treated alloy: (a) basal slip $\langle\bar{a}\rangle$ (b), prismatic slip $\langle\bar{a}\rangle$, (c) pyramidal slip $\langle\bar{c}\rangle$, and (d) pyramidal slip $\langle\bar{c} + \bar{a}\rangle$.

3.3. Mechanical properties

Fig. 7(a) and (b) shows the tensile curves and values of the tensile properties of PM-TA15 alloys under different sintering temperatures and after hot rolling and heat treatment. As shown in the curves, the sintering temperature played a crucial role in the properties containing strength and plasticity of the as-sintered samples. The strength was increased, and the plasticity first increased and then decreased with increasing sintering temperatures from 1200 to 1350°C. At 1300°C, the as-sintered sample possessed better plasticity, which possessed 1002 MPa of ultimate strength, 892 MPa of yield strength, and 10.0% of elongation, which was similar to that of the traditional forging-TA15 alloy. At 1200°C, the lower strength and poor plasticity resulted from the unclosed residual craters, and the existence of these craters made the alloy unable to withstand larger external loads, resulting in poor load transfer stability. The elimination of craters at high temperatures increased the bearing area and the continuity of the microstructure, which prevented the uniform deformation of the alloy from being terminated early due to local strain concentration [29]. At 1350°C, the grains were coarsened significantly, and the density and plasticity of the alloy were reduced. After high-temperature hot rolling, the strength of the alloy reached 1190 MPa, which was considerably higher than that of the as-sintered alloys and the traditional forging-TA15 alloy. The ultimate strength, yield strength, and elongation of the PM-TA15 plate after heat treatment reached 1247 MPa, 1003 MPa, and 14.0%, respectively; the increases for PM-TA15 alloy at 1300°C were 24.5%, 12.4%, and 40.0%, respectively; the increases for forging-TA15 alloy were 27.8%,

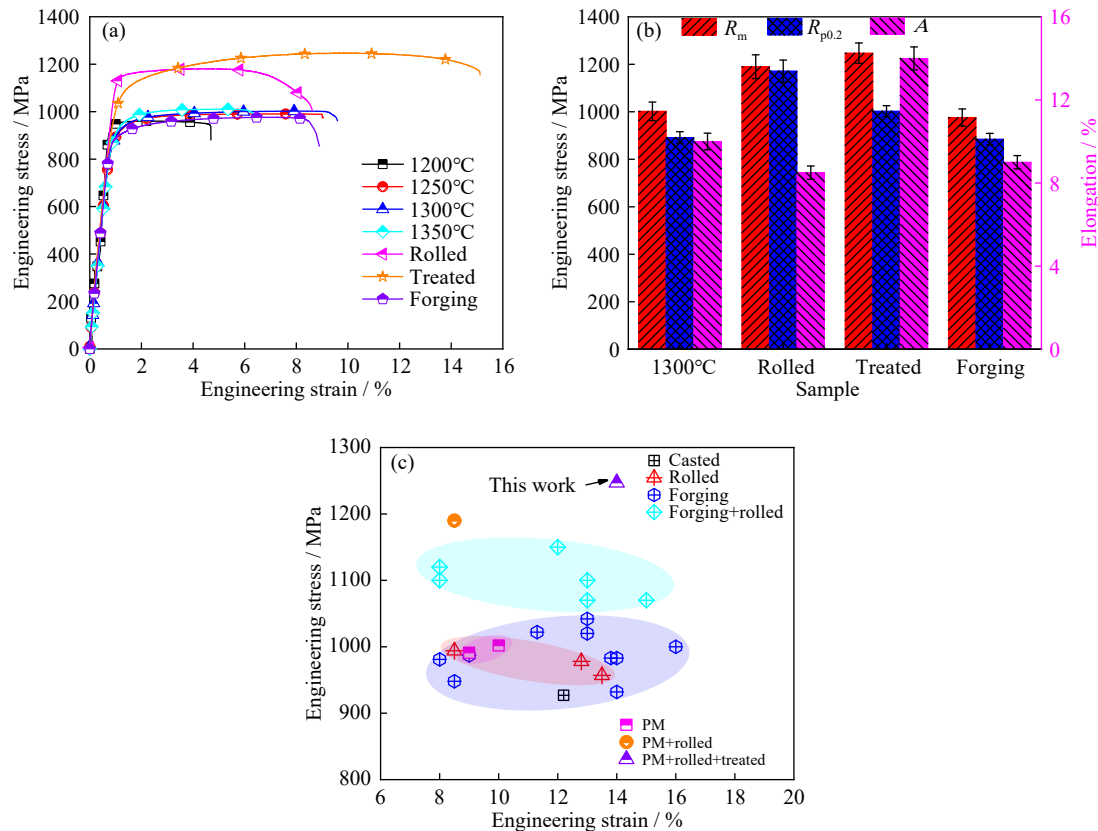


Fig. 7. Tensile properties of PM-TA15 sintered, rolled, and heat treated samples at 20–25°C: (a) tensile curves, (b) tensile values, and (c) comparison of tensile properties. R_m —tensile strength; $R_{p0.2}$ —yield strength; A —elongation.

13.3%, and 55.6%, respectively. Meanwhile, the tensile sample of the as-treated plates showed obvious necking morphology, demonstrating its better plasticity. The tensile properties at 20–25°C of PM-TA15 alloys fabricated in this study complied with the national standard requirements of GB/T 38916-2020, where the requirements in ultimate strength, yield strength, and elongation for TA15 alloy were 930–1130 MPa, ≥ 855 MPa and 6%–12%. Fig. 7(c) compares the ultimate strength and elongation at 20–25°C of TA15 titanium alloys under different preparation processes connected with this study [30–36]. The performance of PM-TA15 sintered billets in this study was superior to that of traditional melting and casting blocks, which was comparable to that of tradi-

tional forging or hot rolling samples. The strength and plasticity of the PM-TA15 alloy after hot rolling and heat treatment were substantially improved, which were superior to those of traditional alloys, such as forging and forging combined with rolling.

Fig. 8 shows the fracture morphology of PM-TA15 alloys after tensile testing. Some residual craters could be clearly observed in Fig. 8(a), which severely affected the plasticity of the alloy sintered at 1200°C. In contrast, the craters in the alloy at 1300°C were closed, and the morphology of the dimples and tear ridges was clearly visible (Fig. 8(c)), which belonged to a typical ductile fracture mechanism. The microstructure was completely refined, and the fracture morpho-

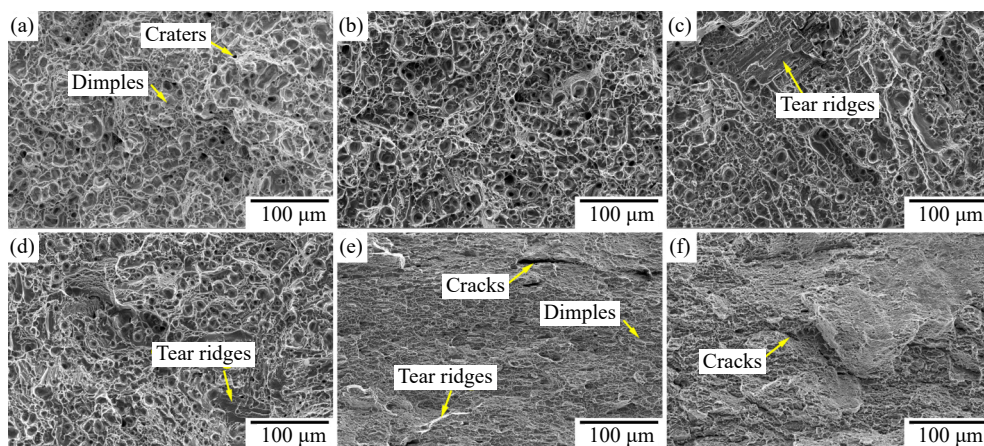


Fig. 8. Fracture morphology of the PM-TA15 sintered, rolled, and heat treated samples: (a) 1200°C, (b) 1250°C, (c) 1300°C, (d) 1350°C, (e) as-rolled, and (f) as-treated.

logy contained more, deeper, and finer dimples and tear ridges in the as-rolled (Fig. 8(e)) and as-treated samples (Fig. 8(f)), which was attributed to the better uniform deformation ability of the as-treated alloy.

Fig. 9 shows the work hardening curves with the true strain of the PM-TA15 alloys. Except for the alloy after hot rolling, an obvious work hardening rate platform existed in the sintered samples at 1300°C, treated samples, and forging-TA15 samples, indicating better uniform deformation ability. The oblateness of the engineering stress–strain curve (Fig. 7(a)) could also confirm this deformation behavior. However, there were significant differences in the working hardening rate of the alloys. The strain platform of the alloys after hot

rolling was shorter, and the short and fluctuating platform resulted from the residual internal stress after the larger hot rolling deformation. As mentioned, the platform of the as-treated sample was longer than that of the other samples, which was related to better plasticity. Meanwhile, except for the rolled sample, the strain curves of the other alloys showed similar trends at the initial strain stage. Additionally, the strain-hardening rate of the traditional forging-TA15 alloy decreased the fastest, and the platform value was reached at a small strain. Meanwhile, the as-treated alloy displayed a slower downward trend, a higher strain-hardening plateau, and a larger platform strain value, indicating better uniform deformation ability.

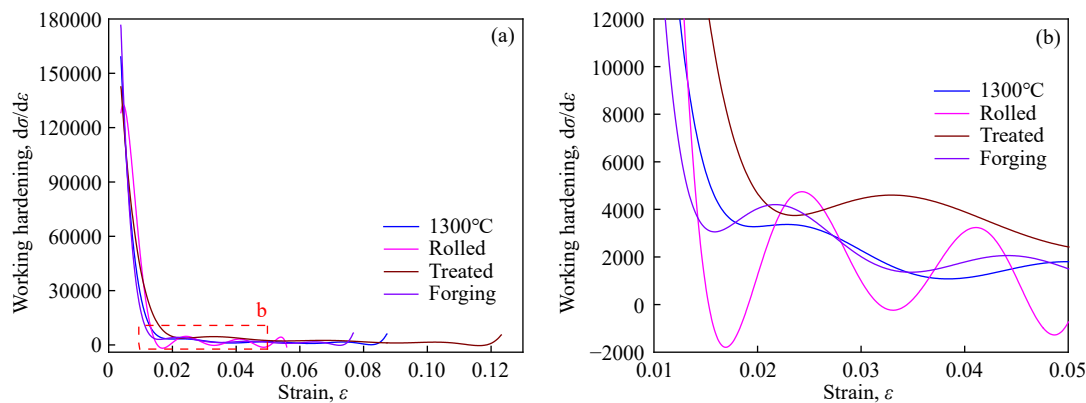


Fig. 9. Working hardening curves of PM-TA15 sintered and rolled samples at 20–25°C: (a) curves and (b) magnified curves. σ —engineering stress; ε —engineering strain.

4. Discussions

As depicted in Fig. 5, the mechanism of microstructural evolution of PM-TA15 alloy under hot rolling relied on dynamic recrystallization (DRX), which was confirmed again by the extremely ultrafine α grains in Fig. 4(b) of the as-treated alloys. Nucleation and growth in traditional recrystallization were caused by the fluctuations of compositions or energy, defined as discontinuous DRX (DDRX). However, titanium alloys with high stacking fault energy tend to have continuous DRX (CDRX), resulting from the accumulation of dislocations in the alloy and substructures surrounded by LAGBs, which further rotate and absorb the dislocations and finally complete the DRX process [37]. Changes related to the local peak of KAM at LAGBs confirmed the presence of CDRX [38], which provided refined grains. Moreover, CDRX was completed by cross-slip of different dislocations rather than the slips alone [39], and the synergistic effect of multiple slip systems provided a good basis for cross-slip for completing DRX. As illustrated in Fig. 6, the as-treated sample possessed positive activity of several slip systems containing a lower CRSS in prismatic slip and a higher SF value in pyramidal slip, which provided better foundations for cross-slip to complete the DRX. Additionally, the splitting peaks could not be observed at 59°–63° in Fig. 4(d), indicating an obvious selection of variants from β to α transformation in hot rolling. This is attributed to the lower cooling rate after hot rolling, resulting in a greater difference in the nucleation activation energy of the α variants. The PM-

TA15 alloy has already transformed into the β -Ti phase with random crystalline orientation after densification and sintering at a higher temperature (1200–1350°C) than the phase transition temperature (\sim 1050°C). Meanwhile, the α -Ti in the treated sample had a specific texture resulting from its limited slip systems, in which the crystalline orientation has been indicated in Fig. 4(a1) and (b1).

The deformation ability of titanium variants was quite different, and the difference in strain distribution led to geometrically necessary dislocations at the lamellar interface to alleviate the uneven deformation, thus providing attached strength to the alloy [40–41]. In this study, the hot rolling temperature, which was much higher than the β phase transition temperature, provided a greater driving force for DRX. During the phase transition from high-temperature to low-temperature, the nucleation of lamellar α was always accompanied by the generation of new phase interface and strain energies. Therefore, the lamellar α preferentially nucleated at the high-temperature β boundary to reduce the strain energy. As illustrated in Fig. 4(a) and (c), the microstructure of the PM-TA15 sample sintered at 1300°C was compact, uniform, and dense. Additionally, smaller grains accompanied by LAGBs, high KAM, and several light gray lines or spots (Fig. 4(b) and (d) and Fig. 5(b) and (d)), which resulted from dislocation entanglement and rearrangement in the grains during hot rolling, forming the substructure. These grain boundaries continuously absorbed dislocations to form DRX, and α -Ti nucleated uniformly and formed refined lamellae through sufficient diffusion because of the relatively slow air

cooling rate. Therefore, the as-rolled and treated samples had a good strain-hardening and considerably improved strength. The improvement of plasticity in the deformed structure was multifaceted. In each small lamellar colony of the as-treated sample (Figs. 4(b) and 5(b)), the orientation of the lamellar α was nearly the same, indicating that the orientation of the adjacent grains accorded with the Burgers orientation relationship. This type of interface made it easy for dislocation accumulation to slip rather than premature microcracking [42–43], thus improving the plasticity of the as-treated sample. Meanwhile, the slip systems of the as-treated sample were discussed in Fig. 6. The coexistence of multiple slip systems made it homogeneous on deformation. For titanium alloys with a less effective slip system, activating deformation twins with better smoothness also played a crucial role in obtaining better plasticity [42].

It has been confirmed that the hot rolling deformation of PM-TA15 treated samples at high temperatures originated from the synergistic effects of different slip systems. Moreover, several slip systems have been activated connected with higher average values of SF (Fig. 6), which resulted from the larger resolved shear stress than the CRSS [27]. The pyramidal slip systems act as the predominant slip mode, which plays an incremental role in the tensile properties along the RD connected with higher tensile strength and plasticity (Fig. 7(a) and (b)). In the tensile process of the PM-TA15-treated sample at 20–25°C, work hardening occupied the main mechanism with few activated slip systems under lower strain, resulting in an increase in the tensile strength [27,30–31]. Additionally, the basal and prismatic slip systems could not complete the deformation, which was limited by the number of independent slip systems in the near- α titanium alloys with high stacking fault energy under large strain. The pyramidal slip system was activated to complete the plastic deformation and delay the occurrence of fracture failure [30–31,35]. As mentioned above, the work hardening behavior of the samples was obviously different with respect to the initial strain-hardening rate, length, and value of the strain platform (Fig. 9). Below a strain of 0.025, work hardening occupied the main mechanism with the decreasing work hardening rate, which resulted from CDRX and the activation of the slip systems. After a strain of 0.025, the pyramidal slip system was activated and gradually occupied the main mechanism to complete the deformation [30–31,35], and the interaction among dislocation accumulation, twin nucleation, DRX, and work hardening reached equilibrium to maintain the strain platform [35,38,42]. Certainly, PM-TA15 possessed better work hardening behavior than the traditional forging-TA15 alloy based on the strain-hardening rate, length, and value of the strain platform, which originated from the raw materials (oxygen content) and fabrication process [32,37].

5. Conclusions

In this study, elemental powders were used as raw materi-

als to prepare TA15 alloys by PM cold pressing sintering combined with high-temperature hot rolling technology. The effects of sintering temperature on the microstructure morphology, phase compositions, and mechanical properties were investigated. The evolution mechanism of the microstructure and strengthening mechanism of the mechanical properties during hot rolling were simultaneously explored. The main conclusions of this study are summarized as follows.

(1) The combination of elemental powders and PM technology could effectively decrease the preparation cost of titanium alloy. After sintering, the alloy had a lamellar structure and uniform chemical compositions, and increasing the sintering temperature accelerated the closing of the craters. At 1300°C, the density of the alloy reached 98.9%, and the strength and elongation at 20–25°C were 1002 MPa and 10.0%, respectively, which was similar to the performance of traditional forging-TA15 samples and satisfied the requirements of the GB/T 38916–2020 national standard.

(2) The microstructure of the PM-TA15 alloy was significantly refined after hot rolling, and the strength and plasticity of the as-treated sample improved cooperatively after solution and aging. The microstructure of the as-rolled sample was fine, dense, and exhibited obvious fiber orientation. After heat treatment, the grains were fine, dense, and uniform. The ultimate strength and elongation of the as-treated alloy were 1247 MPa and 14.0%, respectively, which increased by 24.5% and 40.0% compared with the as-sintered sample at 1300°C and increased by 27.8% and 55.6% compared with the traditional forging-TA15 sample.

(3) The microstructure evolution of the alloy under hot rolling resulted from CDRX, and the refined lamellae provided more nucleation sites for the generation and accumulation of dislocations. The mechanical properties, including strength and plasticity, of the as-treated alloy were improved by the cooperation of the fine, uniform, and dense recrystallization microstructure and multiple slip systems. Additionally, the pyramidal slip system acted as the predominant slip mode to complete the plastic deformation and delay the occurrence of fracture failure. Different work hardening behaviors of the samples were related to different raw materials, fabrication processes, and heat treatments.

Acknowledgements

This work was financially supported by the National Natural Science Foundation of China (No. 52274359), Guangdong Basic and Applied Basic Research Foundation, China (No. 2022A1515110406), Beijing Natural Science Foundation, China (No. 2212035), the Fundamental Research Funds for the Central Universities, China (Nos. FRF-TP-19005C1Z and 00007718), the Aeroengine Group University Research Cooperation Project, China (No. HFZL2021CXY021), and the State Key Lab of Advanced Metals and Materials, University of Science and Technology Beijing, China (Nos. 2021Z-03 and 2022Z-14).

Conflict of Interest

The authors declare that they have no known competing financial interests or personal relationships that could have appeared to influence the work reported in this paper.

References

- [1] D. Banerjee and J.C. Williams, Perspectives on titanium science and technology, *Acta Mater.*, 61(2013), No. 3, p. 844.
- [2] H.Z. Niu, H.R. Zhang, Q.Q. Sun, and D.L. Zhang, Breaking through the strength-ductility trade-off dilemma in powder metallurgy Ti-6Al-4V titanium alloy, *Mater. Sci. Eng. A*, 754(2019), p. 361.
- [3] N. Soro, H. Attar, X.H. Wu, and M.S. Dargusch, Investigation of the structure and mechanical properties of additively manufactured Ti-6Al-4V biomedical scaffolds designed with a Schwartz primitive unit-cell, *Mater. Sci. Eng. A*, 745(2019), p. 195.
- [4] P. Parvzian, M. Morakabati, and S. Sadeghpour, Effect of hot rolling and annealing temperatures on the microstructure and mechanical properties of SP-700 alloy, *Int. J. Miner. Metall. Mater.*, 27(2020), No. 3, p. 374.
- [5] T.L. Zhang, Z.H. Huang, T. Yang, et al., *In situ* design of advanced titanium alloy with concentration modulations by additive manufacturing, *Science*, 374(2021), No. 6566, p. 478.
- [6] J.Y. Zhang, B.N. Qian, Y.J. Wu, et al., A kink-bands reinforced titanium alloy showing 1.3 GPa compressive yield strength: Towards extra high-strength/strain-transformable Ti alloys, *J. Mater. Sci. Technol.*, 74(2021), p. 21.
- [7] Y. Chong, T. Tsuru, B.Q. Guo, R. Gholizadeh, K. Inoue, and N. Tsuji, Ultrahigh yield strength and large uniform elongation achieved in ultrafine-grained titanium containing nitrogen, *Acta Mater.*, 240(2022), art. No. 118356.
- [8] V. Duz, M. Matviychuk, A. Klevtsov, and V. Moxson, Industrial application of titanium hydride powder, *Met. Powder Rep.*, 72(2017), No. 1, p. 30.
- [9] L.P. Zhu, Y. Pan, Y.J. Liu, et al., Effects of microstructure characteristics on the tensile properties and fracture toughness of TA15 alloy fabricated by hot isostatic pressing, *Int. J. Miner. Metall. Mater.*, 30(2023), No. 4, p. 697.
- [10] S.M. El-Soudani, K.O. Yu, E.M. Crist, et al., Optimization of blended-elemental powder-based titanium alloy extrusions for aerospace applications, *Metall. Mater. Trans. A*, 44(2013), No. 2, p. 899.
- [11] Y.F. Luo, Y.H. Xie, W. Zeng, J.M. Liang, and D.L. Zhang, Microstructure and mechanical properties of Ti-6Al-4V rods fabricated by powder compact extrusion of TiH₂/Al₆₀V₄₀ powder blend, *Metall. Mater. Trans. A*, 50(2019), No. 4, p. 1643.
- [12] Z. Wang, Y.N. Tan, and N. Li, Powder metallurgy of titanium alloys: A brief review, *J. Alloys Compd.*, 965(2023), art. No. 171030.
- [13] D.D. Zhang, L.Y. Bao, Q. Li, J.P. Han, and Y.Y. Chen, Microstructure evolution and properties of powder metallurgy Ti43Al9V0.3Y alloy sheets at different rolling temperatures, *Mater. Sci. Eng. A*, 866(2023), art. No. 144685.
- [14] J.K. Hong, C.H. Lee, J.H. Kim, J.T. Yeom, and N.K. Park, Ti strip properties fabricated by powder rolling method, *Surf. Rev. Lett.*, 17(2010), No. 2, p. 229.
- [15] S. Chikosha, T.C. Shabalala, and H.K. Chikwanda, Effect of particle morphology and size on roll compaction of Ti-based powders, *Powder Technol.*, 264(2014), p. 310.
- [16] G.M.D. Cantin, P.L. Kean, N.A. Stone, et al., Innovative consolidation of titanium and titanium alloy powders by direct rolling, *Powder Metall.*, 54(2011), No. 3, p. 188.
- [17] W.H. Peter, T. Muth, W. Chen, et al., Titanium sheet fabricated from powder for industrial applications, *JOM*, 64(2012), No. 5, p. 566.
- [18] D. Mangabhai, K. Araci, M.K. Akhtar, N.A. Stone, and D. Cantin, Processing of titanium powder into consolidated parts & sheet, *Key Eng. Mater.*, 551(2013), p. 57.
- [19] G.M.D. Cantin and M.A. Gibson, Titanium sheet fabrication from powder, [in] M. Qian and F.H.S. Froes, eds., *Titanium Powder Metallurgy*, Amsterdam, Elsevier, (2015), p. 383.
- [20] K.A. Gogaev, V.S. Voropaev, Y.N. Podrezov, Y.I. Yevych, and A.Y. Koval, The effect of compacting rolling on the properties of titanium powder mill products, *Powder Metall. Met. Ceram.*, 55(2017), No. 11-12, p. 633.
- [21] K.A. Gogaev, V.S. Voropaev, Y.N. Podrezov, et al., Mechanical and fatigue properties of powder titanium strips, obtained by asymmetric rolling, *Powder Metall. Met. Ceram.*, 56(2017), No. 1-2, p. 53.
- [22] J. O'Flynn and S.F. Corbin, Effects of powder material and process parameters on the roll compaction, sintering and cold rolling of titanium sponge, *Powder Metall.*, 62(2019), No. 5, p. 307.
- [23] R.J. Xu, B. Liu, Z.Q. Yan, F. Chen, W.M. Guo, and Y. Liu, Low-cost and high-strength powder metallurgy Ti-Al-Mo-Fe alloy and its application, *J. Mater. Sci.*, 54(2019), No. 18, p. 12049.
- [24] A. Govender, C. Bemont, and S. Chikosha, Sintering high green density direct powder rolled titanium strips, in argon atmosphere, *Metals*, 11(2021), No. 6, art. No. 936.
- [25] Y. Zhou, F. Yang, C.G. Chen, et al., Mechanical property enhancement of high-plasticity powder metallurgy titanium with a high oxygen concentration, *J. Alloys Compd.*, 885(2021), art. No. 161006.
- [26] F.C. Qiu, T. Cheng, Y.C. Song, et al., Achieving superior performance in powder-metallurgy near-β titanium alloy by combining hot rolling and rapid heat treatment followed by aging, *J. Mater. Sci. Technol.*, 171(2024), p. 24.
- [27] Y. Chong, R.P. Zhang, M.S. Hooshmand, et al., Elimination of oxygen sensitivity in α-titanium by substitutional alloying with Al, *Nat. Commun.*, 12(2021), No. 1, art. No. 6158.
- [28] Z.Q. Li, K. Han, H.L. Hou, B.Y. Wang, and Z.H. Hu, Effect of hydrogen on diffusion bonding behavior and mechanism of Ti-6Al-4V alloy, *Rare Met. Mater. Eng.*, 43(2014), No. 2, p. 306.
- [29] H.P. Wu, H.L. Peng, X.F. Li, and J. Chen, Effect of hydrogen addition on diffusion bonding behavior of Ti-55 alloy, *Mater. Sci. Eng. A*, 739(2019), p. 244.
- [30] W.C. Xu, D.B. Shan, Z.L. Wang, G.P. Yang, L. Yan, and D.C. Kang, Effect of spinning deformation on microstructure evolution and mechanical property of TA15 titanium alloy, *Trans. Nonferrous Met. Soc. China*, 17(2007), No. 6, p. 1205.
- [31] Q.J. Sun and X. Xie, Microstructure and mechanical properties of TA15 alloy after thermo-mechanical processing, *Mater. Sci. Eng. A*, 724(2018), p. 493.
- [32] Z.C. Sun, J. Zhang, H. Yang, and H.L. Wu, Effect of workpiece size on microstructure evolution of different regions for TA15 Ti-alloy isothermal near-β forging by local loading, *J. Mater. Process. Technol.*, 222(2015), p. 234.
- [33] Y.G. Zhou, W.D. Zeng, and H.Q. Yu, An investigation of a new near-beta forging process for titanium alloys and its application in aviation components, *Mater. Sci. Eng. A*, 393(2005), No. 1-2, p. 204.
- [34] D.M. Huang, H.L. Wang, X. Chen, Y. Chen, and H. Guo, Influence of forging process on microstructure and mechanical properties of large section Ti-6.5Al-1Mo-1V-2Zr alloy bars, *Trans.*

- Nonferrous Met. Soc. China*, 23(2013), No. 8, p. 2276.
- [35] Z.C. Sun and H. Yang, Microstructure and mechanical properties of TA15 titanium alloy under multi-step local loading forming, *Mater. Sci. Eng. A*, 523(2009), No. 1-2, p. 184.
- [36] W.J. Zhou, Z.C. Sun, S.P. Zuo, H. Yang, and X.G. Fan, Shape optimization of initial billet for TA15 Ti-alloy complex components preforming, *Rare Met. Mater. Eng.*, 40(2011), No. 6, p. 951.
- [37] S.Z. Zhang, J.W. Liu, Q.Y. Zhao, C.J. Zhang, L. Bolzoni, and F. Yang, Microstructure characterization of a high strength Ti-6Al-4V alloy prepared from a powder mixture of TiH₂ and 60Al40V masteralloy powders, *J. Alloys Compd.*, 818(2020), art. No. 152815.
- [38] X.X. Ye, H. Imai, J.H. Shen, *et al.*, Dynamic recrystallization behavior and strengthening-toughening effects in a near- α Ti-xSi alloy processed by hot extrusion, *Mater. Sci. Eng. A*, 684(2017), p. 165.
- [39] Y.X. Li, P.F. Gao, J.Y. Yu, S. Jin, S.Q. Chen, and M. Zhan, Mesoscale deformation mechanisms in relation with slip and grain boundary sliding in TA15 titanium alloy during tensile deformation, *J. Mater. Sci. Technol.*, 98(2022), p. 72.
- [40] Y.F. Wang, C.X. Huang, X.T. Fang, H.W. Höppel, M. Göken, and Y.T. Zhu, Hetero-deformation induced (HDI) hardening does not increase linearly with strain gradient, *Scripta Mater.*, 174(2020), p. 19.
- [41] X.Z. Ma, Z.L. Xiang, T. Li, *et al.*, Evolution laws of microstructures and mechanical properties during heat treatments for near- α high-temperature titanium alloys, *Int. J. Miner. Metall. Mater.*, 29(2022), No. 8, p. 1596.
- [42] L. Lei, Q.Y. Zhao, C. Wu, *et al.*, Variant selection, coarsening behavior of α phase and associated tensile properties in an $\alpha+\beta$ titanium alloy, *J. Mater. Sci. Technol.*, 99(2022), p. 101.
- [43] W. Long, S. Zhang, Y.L. Liang, and M.G. Ou, Influence of multi-stage heat treatment on the microstructure and mechanical properties of TC21 titanium alloy, *Int. J. Miner. Metall. Mater.*, 28(2021), No. 2, p. 296.